



HAL
open science

Deciphering electronic and structural effects in Copper Corrole/Graphene Hybrids

Kerry Wrighton-Araneda, Diego Cortés-Arriagada, Paulina Dreyse, Simon Pascal, Gabriel Canard, Luis Sanhueza

► **To cite this version:**

Kerry Wrighton-Araneda, Diego Cortés-Arriagada, Paulina Dreyse, Simon Pascal, Gabriel Canard, et al.. Deciphering electronic and structural effects in Copper Corrole/Graphene Hybrids. Chemistry - A European Journal, In press, 10.1002/chem.202203175 . hal-03925693

HAL Id: hal-03925693

<https://hal.science/hal-03925693>

Submitted on 5 Jan 2023

HAL is a multi-disciplinary open access archive for the deposit and dissemination of scientific research documents, whether they are published or not. The documents may come from teaching and research institutions in France or abroad, or from public or private research centers.

L'archive ouverte pluridisciplinaire **HAL**, est destinée au dépôt et à la diffusion de documents scientifiques de niveau recherche, publiés ou non, émanant des établissements d'enseignement et de recherche français ou étrangers, des laboratoires publics ou privés.

Deciphering electronic and structural effects in Copper Corrole/Graphene Hybrids

Kerry Wrighton-Araneda,^[a,b] Diego Cortés-Arriagada,^[a] Paulina Dreyse,^[c] Simon Pascal,^[d]
Gabriel Canard,^{*[d]} and Luis Sanhueza^{*[e,f]}

[a] Dr. K. Wrighton-Araneda, Dr. D. Cortés-Arriagada
Programa Institucional de Fomento a la Investigación, Desarrollo e Innovación,
Universidad Tecnológica Metropolitana, Ignacio Valdivieso 2409, San Joaquín, Santiago,
Chile.

[b] Dr. K. Wrighton-Araneda
Universidad Bernardo O'Higgins, Centro Integrativo de Biología y Química Aplicada
(CIBQA), General Gana 1702, Santiago, Chile, 8370854.

[c] Dr. P. Dreyse
Departamento de Química, Universidad Técnica Federico Santa María, Av. España 1680,
Valparaíso, Chile.

[d] Dr. S. Pascal, Dr. G. Canard
Aix-Marseille Univ, CNRS, CINaM, UMR 7325, Campus de Luminy, 13288 Marseille
Cedex 09, France.
E-mail address: gabriel.canard@univ-amu.fr

[e] Dr. L. Sanhueza
Departamento de Ciencias Biológicas y Químicas, Facultad de Recursos Naturales,
Universidad Católica de Temuco, Temuco, Chile.
E-mail address: luis.sanhueza@uct.cl

[f] Dr. L. Sanhueza
Núcleo de Investigación en Bioproductos y Materiales Avanzados (BioMA), Universidad
Católica de Temuco, Av. Rudecindo Ortega 02950, Temuco, Chile.

Abstract. Non-covalent hybrid materials based on graphene and A₃-type copper corrole complexes were computationally investigated. The corroles complexes contain strong electron-withdrawing fluorinated substituents at the *meso* positions. Our results show that the non-innocent character of corrole moiety modulates the structural, electronic, and magnetic properties once the hybrid systems are held. The graphene-corrole hybrids displayed outstanding stability *via* the interplay of dispersion and electrostatic driving forces, while graphene act as an electron reservoir. The hybrid structures exposed an intriguing magneto-chemical performance, compared to the isolated counterparts, that evidenced how structural and electronic effects contributed to the magnetic response for both ferromagnetic and antiferromagnetic cases. Directional spin polarization and spin transfer from the corrole to the graphene surface participate in the amplification. Finally, there are relations between the spin transfer, the magnetic response, and the copper distorted ligand field, offering exciting hints about modulating the magnetic response. Therefore, this work shows that copper corroles emerged as versatile building blocks for graphene hybrid materials, especially in applications requiring a magnetic response.

Keywords: Adsorption; Corroles; DFT calculations; Magnetism; Surface science

Introduction.

Hybrid materials have emerged promisingly because of their unique and outstanding properties in catalysis, optical devices, environmental, medicine, and energy storage^[1-6]. Hybrid materials contain a minimum of two components to associate with their unique physicochemical properties and bind through covalent or non-covalent interaction^[7]. In this context, graphene (G), graphene oxide (GO), doped graphene (DG), and graphene quantum dots (GQDs) have been studied due to their attractive mechanical, electrical, and photophysical properties, which might be synergistically complemented with the preparation of graphene hybrid based materials (GBMs)^[8-10]. Covalently linked GBMs are extensively studied, highlighting the advantage of the graphene moiety on increased stabilities, suitable charge/discharge kinetics and capacities, and increased electron transfer processes towards nonlinear optical properties^[11-14]. Macrocyclic compounds such as porphyrins and phthalocyanines seem attractive candidates to tune up the properties of hybrid materials. G surfaces coated with Co-porphyrins and Fe-phthalocyanines enhanced the electron transfer process, providing highly active materials for oxygen reduction reactions^[15]. Besides, GQDs/Zn-porphyrin hybrids have shown high stability and large electron-conductivity towards photocatalytic degradation of pollutants^[16]. Furthermore, G surfaces coated by π - π stacking using water-soluble phthalocyanines demonstrated large synergism as a photosensitizer suitable for photothermal and photodynamic therapies^[17]. Similarly, porphyrin derivatives coated on GO surfaces have shown remarkable fluorescence quenching processes, indicating mostly a fastback electron transfer process on the studied hybrid, in conjunction with a interaction energy of ~ 1.0 eV^[18,19].

On the other hand, corroles and their metallo-derivatives are of great interest because of their unique photophysical and electrochemical properties^[20–22]. Corroles are analogous to porphyrins but lacking the C₂₀ *meso*-carbon atom at the core structure. The later induces a more contracted core with three NH ionizable groups in the core center. The later stabilizes metal ions in high formal oxidation states, compared to the porphyrin analogous^[23,24], highlighting applications in cancer therapy, sensing, organic electronics, and catalysis^[23,25,34,26–33]. New synthetic strategies for developing corrole derivatives have been proposed, mainly substituted at the *beta*^[23,35,36] and/or *meso*^[23,36,37] positions of the corrole core. Electron-withdrawing *meso*-substituents appear as an excellent strategy to increase the stability of the macrocycle, together with the modulation of the electron density on the core structure of the corresponding derivatives^[38]. Alternatively, the binding of metal cations in the central cavity has also been explored; Fe(IV) and Cu(III)^[39–43] corrole complexes have been recognized as exciting metallo-derivatives, where the corrole moiety acts as a non-innocent ligand. In the particular case of Cu-corroles, this definition implies rearranging the electronic structure of the π -extended macrocycle upon metalation. Accordingly, a partial electron transfer between the metal cation and the corrole structure occurs, stabilizing the formation of a magnetically coupled corrole^{2•-}/Cu(II)[•] radical pair instead of the formal expected Cu(III) cation^[42,44,45]. Thus, quantum chemical calculations show that antiferromagnetic coupling between copper and corroles could be predominant over the formal singlet closed-shell spin state, e.g., the Cu(III) case^[42,46,47]. Few references involving corroles on non-covalent hybrid GBMs are reported. Cobalt corroles supported on graphene-based surfaces have improved catalytic performances towards hydrogen evolution^[48] and oxygen reduction reaction^[33]. This behavior is explained according to the strong π - π interactions in the obtained hybrids, high stability, and the fast electron transfer

on the hybrid. Despite this evidence, a systematic study of the electronic and magnetic properties of copper corroles supported on graphene surfaces remains unexplored.

This work investigated a series of A_3 -copper corroles bearing different fluoroalkyl, fluoroaryl, and vinyl substituents at the *meso* positions as models of electron-withdrawing groups. This investigation included the isolated corroles complexes and their corresponding hybrid systems supported on a pristine graphene nanosheet (**Fig. 1**). The fluorinated substituents of the studied Cu corroles were selected since they promote the stability of the corrole structure and increase the formal high valent character of the metal center^[33,38,48]. Additionally, the nature of the substituents (noted R in **Fig. 1**) was selected to evaluate the effect of the aryl, alkyl, or vinyl skeleton, as well as the rigidity of the corresponding substituent on the stability of non-covalent interactions. Density Functional Theory (DFT) calculations were performed regarding the main parameters controlling the occurrence of graphene-corrole hybrids and the modulation of the electronic and magneto-chemical properties of the corresponding hybrids.

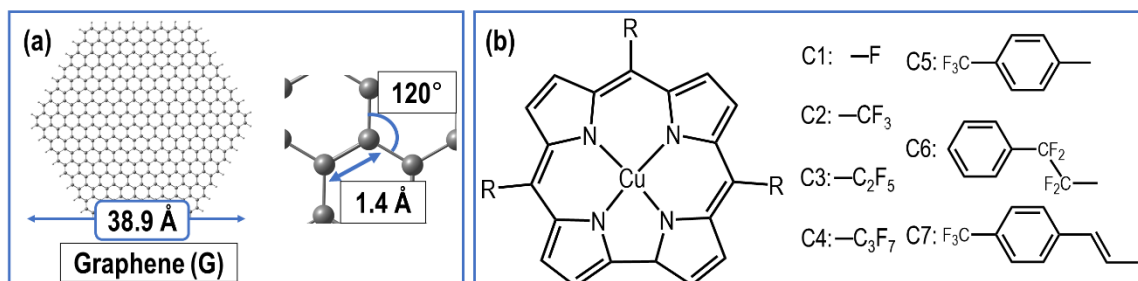


Fig. 1. Molecular structure of (a) Graphene model, (b) R substituent groups, and CuN_4 unit for **C1-C7** compounds.

Results and Discussion.

The stability of copper corroles/graphene hybrids was examined considering the adsorption energy and characterizing their intermolecular interaction. Besides, structural properties, reactivity indexes, and frontier molecular orbitals were discussed. Finally, the

magneto-chemical characterization based on the broken-symmetry approach described the enhanced magnetic response and the spin transfer.

Isolated copper corroles and graphene nanosheet as a platform.

Stability and structural properties of isolated systems.

Firstly, we described the stability of the graphene surface as well as the Cu corroles was determined to be about -7.0 and -5.4 eV, respectively (See **Table S1** for details). In addition, the geometrical parameter of the built graphene nanosheet (**G**), specifically C–C bond lengths and \angle CCC angles, which reach average values of 1.4 Å and 120° , respectively (**Fig. 1a**). The Cu corroles showed different lengths varying from 9.3 to 24.3 Å (**Fig. 2a**) regarding the boundary length of the corresponding substituents linked at the *meso* positions of the corrole core. The obtained geometric parameters of **CuN₄** core in the isolated copper corroles (**C1-C7**) agree with related reported compounds obtained from theoretical and experimental analyses^[42,49,50]. For instance, the studied systems show average Cu–N bond length of 1.9 Å, while \angle NCuN axial angles are $80 - 81^\circ$ and $97 - 98^\circ$ for \angle N₁CuN₁ and \angle N₂CuN₂, respectively (see **Fig. 2b** for general labeling), in correspondence with experimental data summarized in Table S2.

On the other side, considering the non-innocent character of the corrole ligand in this type of complexes, the structure of the corrole core was analyzed based on the torsion angles (α , β , γ , δ , and ψ) to describe the planarity of the corrole macrocycle^[34,46,51]. A detailed analysis of the torsion angles is summarized in Table S1, while and depicted in **Fig. 2b**. The more planar corrole structures were **C3** and **C6**, where the larger torsion angle was β , reaching up to 13° ; this value agrees with other structures found in literature such as CAHYOB and IREVAE crystal structure [codes of Cambridge Structure Database (CSD)].

Conversely, both **C5** and **C7** displayed a significant loss of planarity, showing β torsion angles that reach -46° and -43° , respectively. Similar torsion angles were observed for KAGGIJ and RINCAS crystal structures (CSD codes) in agreement with **C5** and **C7**, respectively, demonstrating the validity of the obtained structures. Thus, **C3** and **C5** are representative cases where planarity distortion depends on the chemical and electronic effect of the *meso* substituents, especially for π -conjugated or aryl groups substituents (**Fig. 2c**). Analogous results were obtained for substituted metallo-corroles described in the literature where the values vary because of steric repulsion of substituents and the metal incorporated in the structure^[34,51–53]. Comparatively, we have calculated g_d value from crystal structures (**Table S2**), with values in the range of 0.185 to 1.206 corroborating a wide variety of distorted structures. For instance, ONUHIQ and KAGGIJ matched with **C5** because the substituents are based on phenyl groups where steric repulsion affect the geometric distortion.

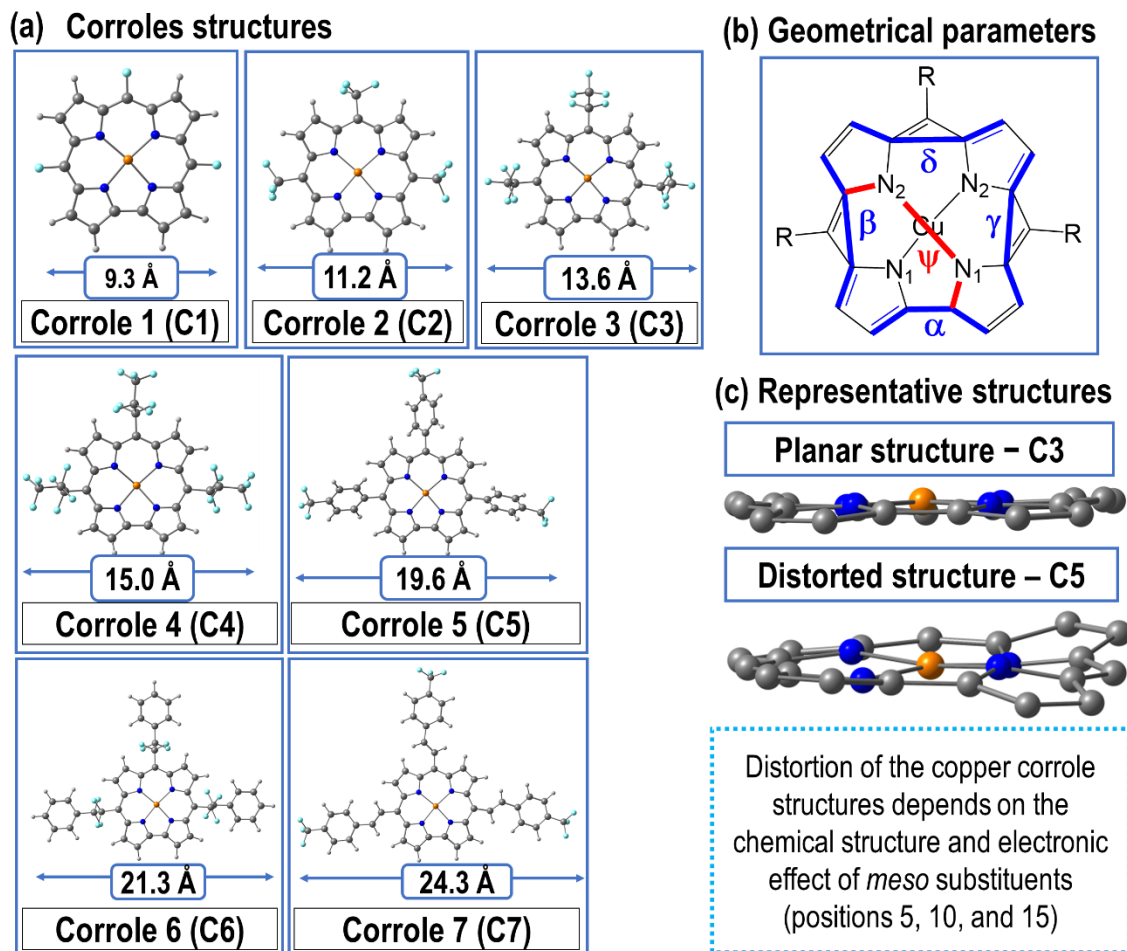


Fig. 2. (a) Molecular length of relaxed geometries for copper macrocycles **C1-C7**. (b) general labeling of the geometrical parameters regarding the core center and dihedral angles representation based on the corrole template (see **Table S1**). (c) representative cases of distorted and planar copper corrole core structures.

Electronic structure and reactivity.

Figure S1 displays the isosurface plots and energies of frontier molecular orbitals (FMOs), including HOMO and LUMO based on open-shell electronic structures (*i.e.*, the α,β spin-orbital functions), while **Table 1** summarizes the main values for the FMOs. As observed, α,β frontier molecular orbitals are located on the corrole core (average value of 93 %), and the R substituents at the 5,15-positions contribute more substantially than the 10-position for **C1** and **C7** systems. The α -orbitals present a higher HOMO–LUMO gap

than the β -orbitals, where the former are 2.2 - 2.7 eV, and the latter is 1.2 - 1.7 eV (α - $\Delta_{\text{HL}} > \beta$ - Δ_{HL} , respectively); in both cases, the α, β - Δ_{HL} overcome the 0.8 eV of graphene nanosheet due to the closed-shell nature of this platform (**Fig. S1**). The global Δ_{HL} values are about 1.9 - 2.1 eV, matching the result with the optical bandgap reported by Agresti *et al.*^[31]. The same tendency of Δ_{HL} has been observed in other DFT calculations of copper corroles substituted in *meso*-positions^[46,49]. Complementarily, **Table 1** summarizes the global indexes considering the chemical potential (μ), molecular hardness (η), and electrophilicity (ω)

Thus, the studied copper corroles display η values of 0.9 - 1.1 eV, suggesting a similar behavior within the studied **CuC** series. The fluorinated case (**C1**) is the harder system because of the direct effect of fluorine atoms over the **CuC** electron structure. The lower η value is found for the alkenyl *meso* substituents (**C7**) because of the π -conjugation of R groups with the **CuC** core, in agreement with the observed FMOs for this compound (**Fig. S1**). As observed in the last row of **Table 1**, the graphene nanosheet presents a considerably lower η value of 0.4 eV, which agrees with the most prominent π -conjugation on the whole surface, providing a planar structure with enhanced electronic polarization.

Table 1. Electronic properties. Δ_{HL} , μ , η , and ω are expressed in eV. Multiplicity ($2\hat{S}+1$), exchange coupling constant (J), and the overlap ($\%S^2$) between corresponding magnetic orbitals. J is in cm^{-1} . g_d is in arbitrary units.

System	Δ_{HL}	μ	η	ω	$2\hat{S}+1$	J	$\%S^2$	g_d
C1	2.2	-4.1	1.1	7.6	3	3	3	0.446
C2	1.9	-4.6	1.0	10.7	3	14	1	0.305
C3	2.0	-4.6	1.0	10.7	3	40	0	0.319
C4	2.0	-4.7	1.0	10.8	1	-20	1	0.300
C5	2.1	-4.2	1.0	8.5	1	-1168	25	0.992
C6	2.0	-4.2	1.0	8.8	3	32	0	0.310
C7	1.8	-4.2	0.9	9.8	3	82	1	0.368

G	0.8	-3.7	0.4	18.1	1
----------	-----	------	-----	------	---

Additionally, the fluorinated alkyl chains in *meso* positions (**C2-C4**) display a more prominent electrophilic character due to the electron-withdrawing effect of these substituents. The electrophilic character is also achieved through π -conjugation in **C7** due to π -conjugation of the trifluoromethylphenyl substituents, which promotes the delocalization of electron density through the whole **CuC** core.

Spin density and magnetic properties.

Regarding the spin density distribution, the Cu center displays values of 0.6 a.u. in agreement with other works related to the magnetic properties of Cu(II) complexes (showing one unpaired electron) ^[54,55]. Besides, the spin density surface (**Fig. S1**) is mainly on the **CuC** core, and the surface shape resembles the $3d_{x^2-y^2}$ orbitals as is proper of Cu(II) center in a square-planar ligand field ^[42,49]. In this sense, part of spin density is localized onto Cu(II). In contrast, the remaining spin density is delocalized along with the corrole core, showing a non-innocent and magnetic character. The energy difference between singlet and triplet (Δ_{t-s}) are included in **Fig. S1**, where negative values described ferromagnetic cases, and positive values for antiferromagnetic cases.

Because of the non-innocent character of the corrole ligand, multiplicity studies were performed to evaluate the spin state of the minimum energy structures showing different values in each case (**Table 1**). The spin density surfaces are plotted in **Fig. S1** according to minimum energy spin states. A ferromagnetic nature is found in compounds **C1**, **C2**, **C3**, **C6**, and **C7**, which display triplet spin-state ($2\hat{S}+1=3$) and positive values of the magnetic exchange constant (J), oscillating between 3 to 82 cm^{-1} . Conversely, an antiferromagnetic ground state is found for compounds **C4** and **C5**. Noteworthy is the

antiferromagnetic behavior of **C5** since it displays the stronger coupling of -1168 cm^{-1} that agrees with the high overlap between α and β unrestricted corresponding orbitals (UCOs), reaching 25 % on the whole molecule (**Fig. 3a**). This overlap is allocated to the Cu center, in contrast to the strong ferromagnetic case (**C7**), showing a negligible overlap on the metal center and reaching only 1.25 % of overlapping on the whole molecule (**Fig. 3b**).

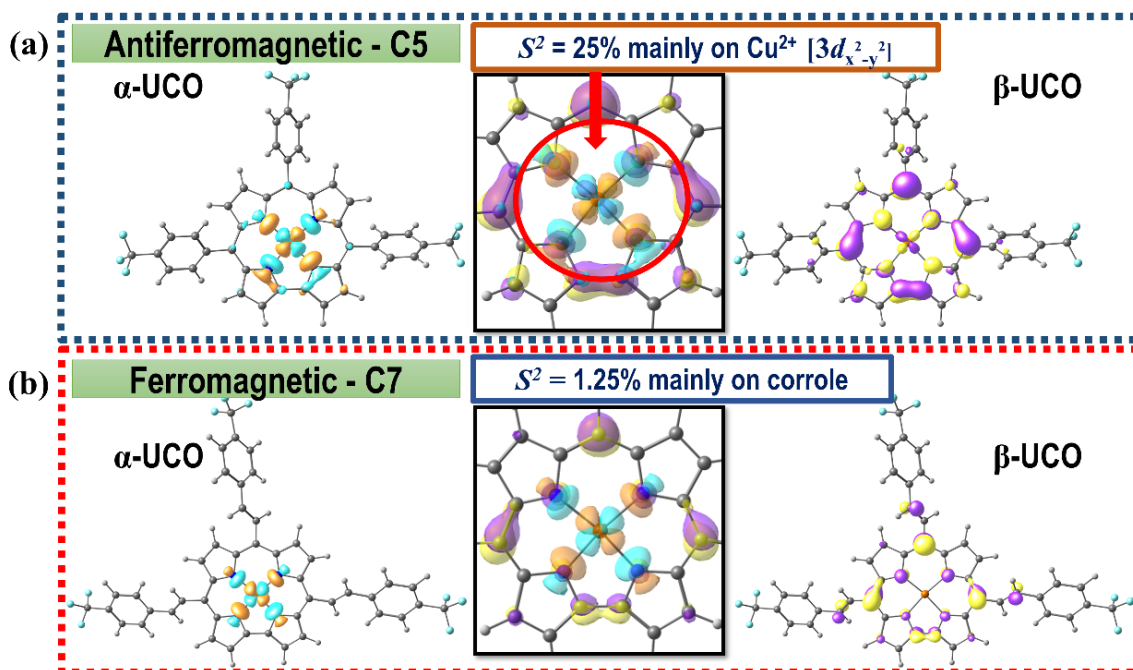


Fig. 3. Representation of unrestricted corresponding magnetic orbital for (a) **C5** antiferromagnetic corrole and (b) **C7** ferromagnetic corrole. Isodensity value of 0.05 a.u. for each surface.

It is necessary to note that the relationship between overlapping magnetic orbitals and the antiferromagnetic nature of the coupling is revisited in Goodenough-Kanamori's model to understand the magnetic behavior of complexes in solid-state^[56,57]. Thus, the orthogonality and overlapping between magnetic orbitals are essential descriptors for exploring magnetic properties from a chemical point of view. Other structural parameters also act onto the orbital orthogonality and overlapping, such as planarity of the ring, which can affect the magnetic exchange between corroles, as found in the literature for bis-copper

corroles^[58]. For this reason, the geometrical distortion (g_d , **Table 1**) of the **CuN₄** core was compared to the symmetric square-plane structure (D_{4h} point group) as a descriptor of the ligand field influence on the magnetic behavior. Thus, the higher g_d value is found for stronger antiferromagnetic coupling in **C5**, reaching almost the unity. Besides, a statistical study to rationalize the magnetic behavior, structural parameters, and electronic properties show correlations of magnetic coupling with α , δ , g_d , and % S^2 , displaying correlation parameters of 0.77, 0.81, 0.95, and 0.99, respectively (**Fig. S2**). Lastly, we highlighted that even the non-innocent character of corroles strongly depends on the planarity of corrole, substituent steric effects, and the metal center^[59], corroborating the significant influence of structural and chemical modification on the electronic properties of corroles.

Hybrid materials corroles-graphene.

Stability and structural properties of C-G hybrids.

Copper corroles are adsorbed onto G in a stacked planar configuration (**Fig. 4**) at distances (d_{stack}) of 3.0 - 3.2 Å and adsorption energy of 2.0 - 3.9 eV (**Table 2**). Therefore, all the **C-G** hybrids are stable via non-covalent bonding. These results agree with non-metallated corroles adsorbed onto oxidized graphene, where a stacked conformation is more stable ($E_{\text{ads}} = 1.4$ eV) than lateral conformation ($E_{\text{ads}} = 0.2$ eV)^[60]. Besides, the stacked conformation has been also corroborated for the corrole adsorption onto metallic surfaces, such as Au(111), Ag(111), and Pt(111)^[49,61-64]. Here, the non-covalent adsorption of corroles and corrolato onto Ag(111) displayed adsorption energies between 2.8 - 4.7 eV, where the π -electron conjugation between radical corroles and the surface increases the stabilization because of aromatic effects^[62].

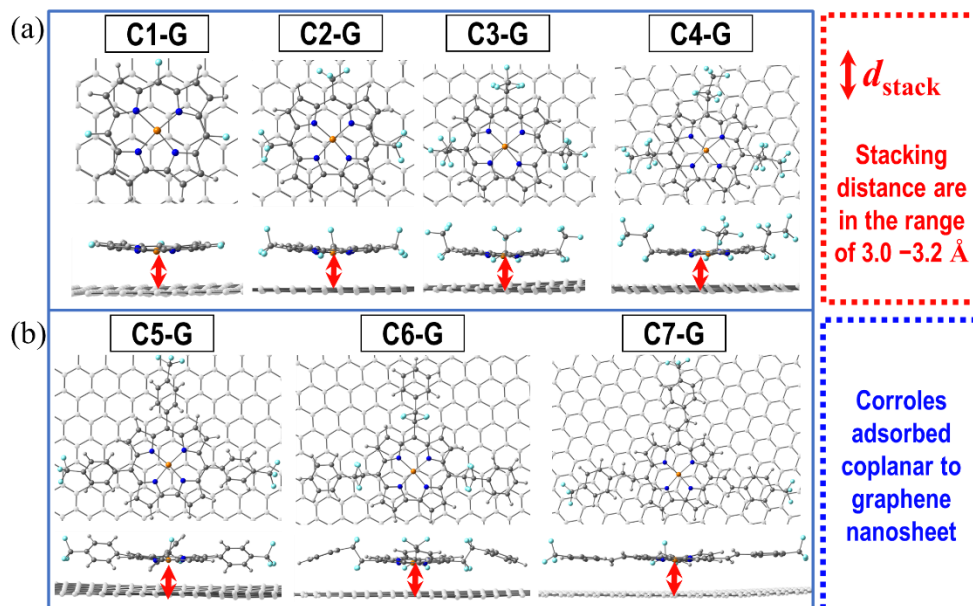


Fig. 4. Relaxed molecular structures of the C-G hybrids (top and side views). (a) Hybrids with non-aromatic substituents and (b) hybrids with aromatic substituents.

Significant correlations were found between E_{ads} , $|\Delta E_{\text{int}}|$, and the number of carbon atoms in each copper corrole (**Fig. S3**). The adsorption energy per carbon atom of corrole (E_{ads}/C) and absolute value of interaction energy per carbon atom ($|\Delta E_{\text{int}}|/C$) displayed an average value of ~ 90 meV/atom and ~ 100 meV/atom, respectively, indicating that more substantial stabilization will be achieved for larger R substituents. For instance, the lower stabilization is obtained for the **C1-G** hybrid, while the more considerable stabilization is reached by the **C7-G** hybrid (E_{ads} and ΔE_{int} in **Table 2**). As counterpart, ΔE_{prep} represents the energy destabilization because of the structural deformation suffered by graphene and copper corroles during the adsorption process. Thus, the hybrids with aromatic substituents reach higher deformation, i.e., the higher ΔE_{prep} values. The latter is associated to the steric effects in the aromatic R substituents compared to the non-aromatic fluoroalkyl substituents, where the latter present a lower rotational barrier (similar to alkyl groups) than π -conjugated groups. For instance, the vinyl group rotation in **C7-G** suffers steric

impediment between phenyl hydrogen atoms and corrole outer hydrogen atoms, while the C=C double bond cannot freely rotate. Thus, the ΔE_{prep} involved in the deformation increases for the aromatic substituents during the stacking process. As an illustration of the structural changes, the torsion angles reflect the increase of planarity of the corrole cores, which can be observed by the decrease of α , β , γ , δ , and ψ angles (see **Table 2**). Thus, the increase of planarity occurs by the electronic interactions with the graphene surface, similar to non-metallated and copper corroles adsorbed onto Au(111) and Ag(111) surfaces^[49,62].

Table 2. Electronic properties of **C-G** hybrids. Charges are expressed in $|e|$, while μ , η , ω , and E_{ads} are in eV.

System	d_{stack}	E_{ads}	ΔE_{int}	ΔE_{prep}	Q_{CT}	α	β	γ	δ	ψ
C1-G	3.0	2.1	-2.3	0.2	0.0	0	-8	10	-1	-1
C2-G	3.1	2.4	-2.6	0.2	0.6	0	-7	9	0	0
C3-G	3.1	2.0	-2.3	0.3	0.8	0	-5	7	-1	2
C4-G	3.2	2.5	-2.6	0.2	0.8	11	-26	-13	16	0
C5-G	3.2	2.9	-3.6	0.6	0.1	13	-26	-2	3	0
C6-G	3.2	3.0	-3.4	0.4	0.0	1	-13	11	1	-3
C7-G	3.1	3.9	-4.3	0.4	0.0	12	-6	-32	20	4

On the other hand, the charge transfer (Q_{CT}) flows from graphene to the copper corroles, where the highest transfer occurs for corroles with non-aromatic fluoroalkyl substituents due to a strong electron-withdrawing effect (**C2-G**, **C3-G**, and **C4-G**). The highest electron transfer reaches 0.8 $|e|$ (copper corroles gain negative charge), showing that the graphene behaves as an electron reservoir. Conversely, the **C1-G**, **C5-G**, **C6-G**, and **C7-G** hybrids showed almost neglectable charge transfer ($Q_{CT} \sim 0|e|$). In this sense, the electron-withdrawing effect of non-aromatic fluoroalkyl substituents supports the charge movement from graphene; nonetheless, the charge transfer is not the dominant influence on the stabilization mechanism of **C-G** hybrids since no correlation between Q_{CT} and E_{ads} is observed.

In this regard, we have explored the nature of chemical bonds using the AIM method to detect specific interactions between both components. However, the extended number of intermolecular interactions present values of ρ_{BCP} in the range of 0.001 – 0.013 $|e/\text{Bohr}^3|$, indicating that weak electrostatic interactions drive the stabilization. Nonetheless, the interaction mechanism in **C-G** hybrids should be also driven by Van der Waals forces derived from π -conjugation of corroles interacting with graphene in a parallel displaced π -stacking. With this in mind, the non-covalent interactions were explored using the independent gradient model to characterize pictorially the dispersive driving force (**Fig. 5**, see **Fig. S4** for all **C-G** systems). The regions of high stabilization [red colored for $\text{sign}(\lambda_2)\rho$ negative values] are located below fluorine and H- π interactions form stabilizing interactions, while subtle stabilizing regions are located below copper and nitrogen atoms that belong to **CuN₄** core (**Fig. 5**). Conversely, repulsive interactions [blue colored for $\text{sign}(\lambda_2)\rho$ positive values] between Cu–N bonds and graphene are observed, especially the most intense steric repulsion is observed between twisted phenyl group and graphene nanosheet in **C5-G** hybrid. Considering IGM surface sizes, there is some correspondence with the E_{ads} tendency since **C5-G**, **C6-G**, and **C7-G** hybrids are the more stable systems. The latter can be explained considering that the sum of an extended number of low stabilizing interactions achieves a valuable contribution to the whole stabilization. This point suggests that the dispersion forces are the main driving forces for the interaction of **C-G** hybrids.

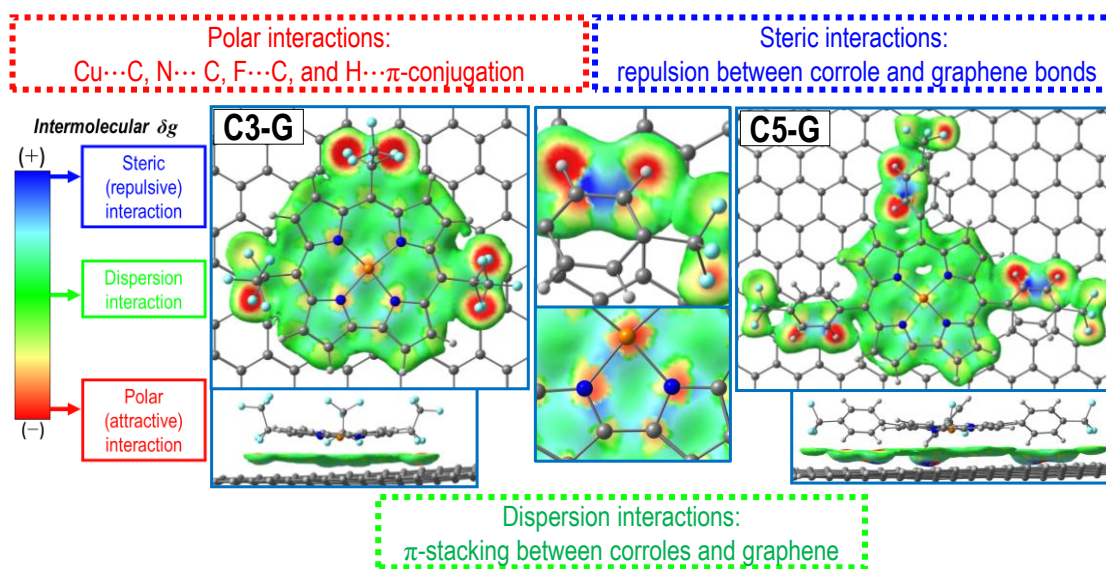


Fig. 5. Molecular isosurfaces based on intermolecular IGM for **C-G** hybrids. $\delta g^{\text{inter}}=0.005$ a.u., color coding in the electron density range $+0.025 > \text{sign}(\lambda_2)\rho > -0.025$ a.u. (map region in blue and red color, respectively)

Electronic structure and reactivity of C-G hybrids

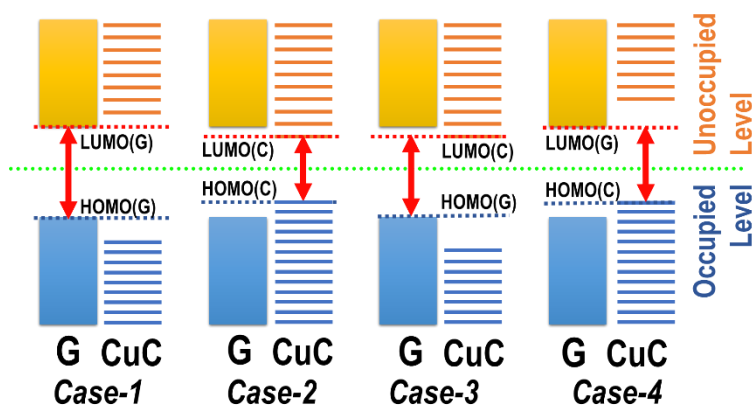
The electronic structure of **C-G** hybrids is revised regarding the FMOs surfaces for α,β -frontier molecular spin-orbitals, and the global reactivity descriptors (**Fig. S5** and **Table 3**). The energy difference between singlet and triplet (Δ_{t-s}) are included in **Fig. S5**, where ferromagnetic cases are the most favored cases reaching up to 648 meV (~63 kJ/mol).

In the **C-G** hybrids, the copper corroles participate more actively for the α,β frontier molecular spin-orbitals, in contrast with the isolated copper corroles. This kind of distribution has been reported previously for the adsorption studies of 2D nanomaterial^[65]. Indeed, as also summarized in **Scheme 1**, four different cases are observed for the α,β - Δ_{HL} depending on the corroles participation:

- 1) *the HOMO/LUMO pair is located both onto graphene [HOMO(G)/LUMO(G)] displaying HOMO-LUMO gaps of 0.7 - 1.2 eV. In this case, the graphene*

HOMO-LUMO energies are contained into the range of the corrole HOMO-LUMO energy.

- 2) *the energy of HOMO/LUMO pair is distributed onto copper corrole [HOMO(C)/LUMO(C)] and displays a value of 0.3 eV, e.g., α -HOMO(C2)/LUMO(C2). The corrole HOMO-LUMO energies are contained into the range of graphene HOMO-LUMO energy.*
- 3) *the HOMO(G)/LUMO(C) pair shows α, β - Δ_{HL} values of 0.5 - 0.7 eV. This case occurs when corrole LUMO energy is between graphene HOMO-LUMO energies range. That is, corroles introduce a vacant orbital between graphene's HOMO-LUMO.*
- 4) *the HOMO(C)/LUMO(G) pair presents the lower gaps between 0.1 - 0.3 eV. This case occurs when corrole HOMO energy is between graphene HOMO-LUMO energies. In other words, corrole introduced an occupied orbital between HOMO-LUMO energy.*



Scheme 1. Representation of case-1, case-2, case-3, and case-4 regarding energy states in copper corroles–graphene hybrids.

For instance, **C3-G** hybrids can be classified as *case-4*, displaying low global Δ_{HL} values of 0.1 eV. In contrast, the **C5-G** hybrid is a mixture of *case-1* and *case-3*, reaching up to 0.9 eV, close to the isolated graphene nanosheet ($\Delta_{\text{HL}}=0.8$ eV, **Table 1**) in correspondence with a significant contribution to the α and β spin-orbitals.

Table 3. Electronic properties of **C-G** hybrids. Δ_{HL} , μ , η , and ω are expressed in eV.

System	Δ_{HL}	μ	η	ω
C1-G	0.7	-3.7	0.4	19
C2-G	0.5	-3.9	0.2	31
C3-G	0.1	-3.8	0.1	123
C4-G	0.2	-3.8	0.1	59
C5-G	0.9	-3.8	0.5	16
C6-G	0.6	-3.8	0.3	23
C7-G	0.7	-3.7	0.3	21

Comparatively, the reactivity is in line with the participation of the fragment involved in frontier molecular spin-orbitals. For instance, **C1-G**, **C5-G**, **C6-G**, and **C7-G** hybrids present close to 75 % of graphene participation in the Frontier Molecular Orbitals, preserving graphene's reactivity descriptors ($\mu = -3.7$ eV, $\eta = 0.4$ eV, and $\omega = 18.1$ eV). On the other hand, for **C2-G**, **C3-G**, and **C4-G** hybrids, the corrole moiety introduces orbitals between graphene's conduction and valence bands, thus decreasing the Δ_{HL} and η , while ω increases substantially. Considering the relation between Δ_{HL} with optic and conducting properties, the *case-3* and *case-4* outstand by the opportunity of the generation of electron mobility employing light stimuli. For example, in the *case-3*, light can promote electron density from **G** to **CuC** employing only ~ 1700 nm (0.7 eV according to results). While the *case-4* displays the lowest values of Δ_{HL} suggesting a conductor behavior between **G** and **CuC** pair. Thus, the results suggest a wide versatility of **CuC** developing chemical

modifications of the substituents as an invitation to evaluate the optic, conduction, and sensing applications.

From a structural point of view, changes in the planarity substantially affect the orbital structure of metallo-macrocycles. Because of their planar structure, the orbitals of copper are orthogonal to the π -conjugation of corrole, favoring the formation of d- π hybrid orbitals. Besides, the increase in planarity supports the π - π stacking with graphene-based surfaces^[66]. The frontier molecular spin-orbitals are also affected in other examples of corroles adsorbed onto Au(111), Ag(111) and Cu(111) surfaces^[49,62,63,67]. Experimentally, these changes could be observed using scanning tunneling microscopy (STM) and Kondo resonance; nevertheless, the main effects are linked to the magnetic properties.

Magneto-chemical properties

Regarding the magnetic properties of the **C-G** hybrids, the unpaired electrons can be distributed within the whole system, including the graphene platform. Indeed, the spin density surface of **C-G** hybrids is mainly allocated on both copper corroles and the edge of the graphene nanosheet (**Fig. S5**). Certainly, spin density delocalization/polarization mechanism is present in all the cases that agree with other studies, especially for graphene nanoribbons^[68,69]. On the other side, it is essential to differentiate the charge transfer (Q_{CT}) vs. spin-transfer phenomena since the spin density (ρ_S) is the difference between α and β spin density: $\rho_S = \rho_\alpha - \rho_\beta$. In this sense, the Q_{CT} parameter does not differ between α and β electrons, but spin density transfer can occur with $Q_{CT} = 0$ if the spin density location is balanced^[49,70]. In the cases of **C2-G**, **C3-G**, and **C4-G** hybrids, the charge transfer/spin density delocalization coincides, analogous to forming a transient corrole radical due to an electron transfer^[62], in other words, the formation of compensated spin polarized that is

dissipated through the graphene. Similarly, there is reported that Ag(111) surface transfers electron and spin density to corroles due to dispersion and aromatic driving forces^[62]. In this sense, we propose the aromatic character of the fragment of the **C-G** hybrid arises as other stimuli to reach higher magnetic coupling.

Since the spin density is allocated on graphene, this effect modified the magnetic behavior substantially. The spin-transfer occurs on **G** by the interaction with corroles. By analogy with Q_{CT} , the spin-transfer (ρ_{ST}) can be quantified summing the atomic spin density of each atom that compose a fragment. In this sense, the ρ_{ST} of the **G** fragment will reveal how corroles can generate a magnetic response over the platform. The ρ_{ST} values suggest an integer spin is transferred to graphene (**Fig. 6a**). For instance, no spin-density is transferred for **C1-G**, and **C6-G** hybrids; close to one spin was transferred for **C2-G**, **C3-G**, **C4-G**, and **C5-G** hybrids, while two spins were transferred to **C7-G** hybrid. Because of the π -conjugated character of graphene, the spin density is delocalized along the nanosheet, but a directional spin polarization is observed, especially for the ferromagnetic hybrids (**Fig. 6b** and **Fig. S5**). Note that this *directional spin polarization onto the edges of the G sheet* can be mostly related to a limitation of the molecular nature of the model used in the calculations, since the presence of hydrogen atoms at the edges of the **G** sheet eventually modify the spin density onto the **G** sheet. As observed in **Figure S6**, an important spin density is transferred onto the graphene surface (including the 288 C atoms in the **G** sheet) in the ferromagnetic state, with 1.4 electrons, according to the Mulliken and Hirshfeld population analyses. In this regard, the periodic calculations for this model are in complete agreement compared to the molecular model, in terms of an evident spin transfer onto the **G**

sheet, and where the molecular model redistribute the spin density onto the edges mostly due to the nature of the model.

Despite this observation, this interpretation should be associate more a spin transfer onto the whole **G** sheet than a specific allocation of the corresponding transferred electrons. Interestingly, correlations were observed when comparing the geometrical distortion of **CuN₄** core (g_d) with spin transfer (**Fig. S7**). Besides, the stability descriptors are also related to spin-transfer, since electronic hardness (kinetic stability), and adsorption energy (thermodynamic stability) show significant correlation parameters (**Fig. S8**). These results suggest that the spin transfer process is associated with the structural and electronic properties of the copper corroles, showing that the spin transfer to graphene is a complex process that involves several variables.

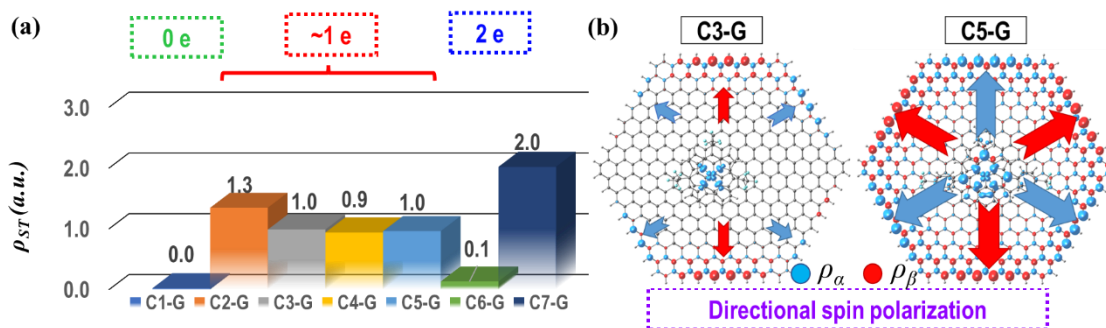


Fig. 6. (a) Spin transfer for **C-G** hybrids. (b) spin density surface for **C3-G** and **C5-G** hybrids. Isodensity value of 0.003 a.u. for each surface.

The magnetic response of most systems increases in terms of the absolute value, being the ferromagnetic nature more strongly favored. The **C5-G** hybrid shows the stronger ferromagnetic coupling of $+3316 \text{ cm}^{-1}$ without overlap between corresponding magnetic orbitals (**Table 4**). The strong ferromagnetism agrees with the low overlap between magnetic orbitals and the increase of planarity for copper corroles since the planarity of the

corrole ligand supports the π -conjugation where the orbitals are orthogonal to the $3d_{x^2-y^2}$ proper of Cu(II) centers stabilizing the ferromagnetic states. Conversely, the **C3-G** hybrid displays a more robust antiferromagnetic behavior with -1869 cm^{-1} and a high % S^2 of magnetic orbitals reaching up to 63%. Comparatively, a set of copper corroles adsorbed on Au(111) reported magnetic couplings between -909 to $+1784 \text{ cm}^{-1}$, suggesting that the magnetic properties of copper corroles are highly modulable by incorporating new substituents^[49]. These magnetic behaviors were reported for silver corroles where π -conjugation also interacts with the $4d_{x^2-y^2}$ orbital of Ag(II), but the higher torsion angles in the distorted structure obstruct the ferromagnetic coupling. Consistently, a previous study reported the strong antiferromagnetic coupling of non-metalated corroles adsorbed onto Ag(111), reaching up to -2371 cm^{-1} ^[63].

Table 4. Magnetic properties of **C-G** hybrids and copper corroles employing the hybrid geometry (**C***). Multiplicity ($2\hat{S}+1$), exchange coupling constant (J), and the overlap (S^2) between corresponding magnetic orbitals. J is expressed in cm^{-1} .

System	$2\hat{S}+1$	J	$\%S^2$	System	$2\hat{S}+1$	J^*	$\Delta\hat{S}$	ΔJ
C1-G	3	1267	<0.01	C1*	3	214	0	1053
C2-G	3	2003	0.56	C2*	3	1168	0	835
C3-G	1	-1869	63.38	C3*	1	-364	0	-1505
C4-G	3	1470	7.89	C4*	3	883	0	587
C5-G	3	3316	0.03	C5*	3	100	0	3216
C6-G	3	13	0.38	C6*	3	14	0	1
C7-G	3	824	3.14	C7*	1	-106	1	940

The characterization of the corresponding magnetic orbitals evidences the exchange pathway between the magnetic centers. In fact, the **C5-G** hybrid out stands by the substantial magnetic response because of the high stabilization of the high-spin state (triplet state) with a corresponding diminished overlap between α, β -UCOs. Indeed, the surface of α -UCO is allocated onto corroles while β -UCO is distributed on graphene, thus with a very

limited contact between both magnetic orbitals (**Fig. 7a**), and the unpaired electrons poorly interact by a direct magnetic pathway. On the contrary, the **C3-G** hybrid displayed strong antiferromagnetism with high α,β -UCOs overlap (63%), which occurs on graphene and not on the **C-G** hybrids (**Fig. 7b**). Indeed, the unpaired electrons can interact antiferromagnetically through the exchange pathway with no resistance. Considering the current evidence, the graphene nanosheet is presented as a platform able to act as an amplifier of the magnetic response that directs/conducts the spin transfer through its structure.

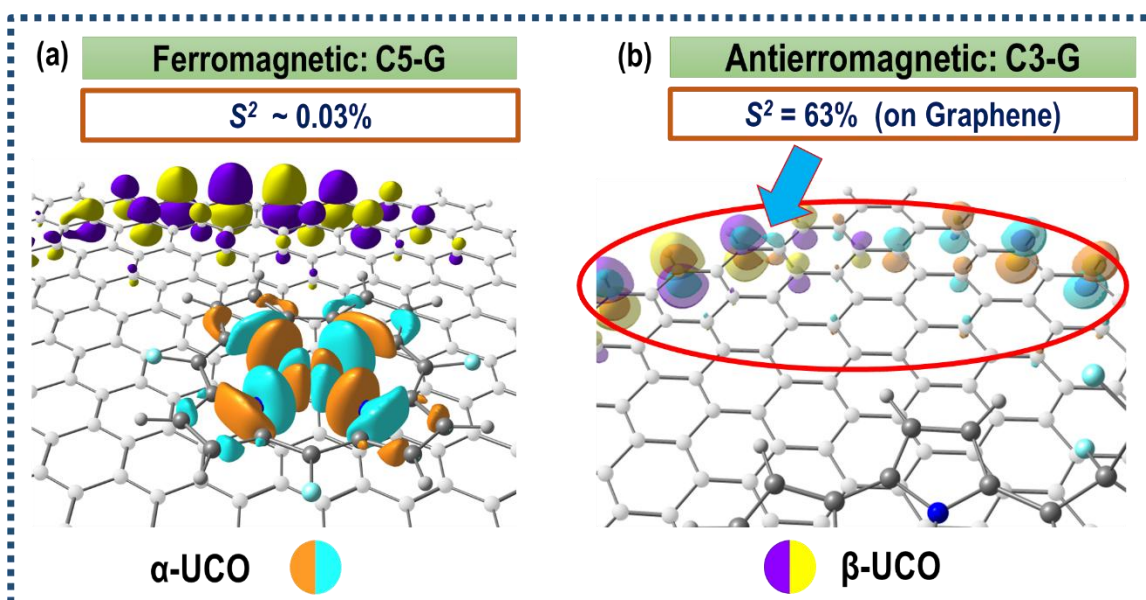


Fig. 7. Representation of unrestricted corresponding magnetic orbital for (a) **C5-G** hybrid and (b) **C3-G** hybrid. Isodensity value of 0.025 a.u. for each surface.

However, it is necessary to decipher if the current magnetic behavior is part of structural changes, spin-transfer phenomenon, or this behavior results from the synergistic effect between the properties mentioned above. For this purpose, the magnetic properties of copper corroles keeping the geometry of **C-G** hybrids were evaluated and marked with the “*” symbol. Besides, the change in the coupling constant (ΔJ) and magnetic moment variation ($\Delta \hat{S}$) were calculated as follow: $\Delta J = J - J^*$; $\Delta \hat{S} = \hat{S} - \hat{S}^*$ (**Table 4**). These

descriptors are addressed to evaluate the effect of the interaction between graphene nanosheet and the **CuC**. For example, if $\Delta\hat{S}=0$, no magnetic reversion occurs, while $\Delta\hat{S}=1$ shows a reversion of the magnetic nature. Moreover, if $\Delta J = 0$, no magnetic changes occur; $\Delta J > 0$ implies a ferromagnetic contribution, and $\Delta J < 0$ reveals antiferromagnetic contribution due to the interaction with graphene nanosheet. With this in mind, the magnetic properties of copper corroles showed a ferromagnetic contribution of graphene for **C1-G**, **C2-G**, **C4-G**, **C5-G**, and **C7-G** hybrids, suggesting an amplification of the magnetic response rising to $\Delta J = 3216 \text{ cm}^{-1}$. Whereas the **C3-G** hybrid presented an antiferromagnetic contribution of -1505 cm^{-1} , the **C6-G** hybrid is almost not affected by the interaction with graphene. Last, the reversion of the magnetic nature only occurs in **C7-G** since this hybrid becomes ferromagnetic during the interaction with graphene. Therefore, the graphene nanosheet can affect the magnetic response in two ways: (i) affecting the structural array during the adsorption process and inducing planarity to copper corroles; (ii) offering an electronic platform to amplify the magnetic response by spin transfer. Thus, graphene actively stabilizes the hybrids and changes the structural, electronic, and magnetic properties of **C-G** hybrids.

The magnetic properties were compared with structural and electronic properties. A strong correlation between the electrophilicity and the overlap of corresponding magnetic orbitals (S vs. ω plot in **Fig. S8**) suggests that a more considerable overlap supports the stabilization of additional electron density. The ΔJ and ω correlations shows that high electrophilic **C-G** hybrids support the augmented antiferromagnetic response (ω vs. ΔJ plot in **Fig. S8**). That is why the **C3-G** hybrid presents the augmented antiferromagnetic response after adsorption. Similar analysis shows that the geometrical distortion of the **CuN₄** (in isolated copper corroles) and its variation concerning **C-G** hybrids (g_d and Δg_d ,

respectively) is involved in the augmented magnetic response in the graphene interaction (plots relative to ΔJ in **Fig. S8**). In consequence, the explanation of the augmented magnetic response of **C-G** hybrids is consistent with the magneto-chemistry either by analyzing the chemical structure, the electronic properties, the corresponding magnetic orbitals, and the respective hybrid stabilization during the adsorption process.

Concluding remarks.

In summary, a series of non-covalent hybrid systems based on fluorinated A₃-type copper corrole complexes adsorbed on a pristine graphene sheet was studied by DFT calculation. The results showed the hybrids display significant stabilization with adsorption energies between 2.0 and 3.9 eV. This stabilization is favored by a π - π stacking with distances of 3.1 Å between both fragments, where graphene behaves as an electron reservoir for the most conductive cases. A significant flattening corrole ligand accompanies the formation of the corresponding hybrid, compared to the isolated counterparts. Summarizing (i) the geometrical rearrangement of the corroles during the adsorption onto graphene could be induced by weak electrostatic interactions and dispersion forces, (ii) *meso*-substituents affect the electronic properties of the hybrids, especially kinetic stability based on the electronic hardness of the corresponding systems. (iii) Graphene modulated the reactivity of the hybrid systems displaying active participation in the HOMO and LUMO; the lowest reactivity was observed to hybrids with a more significant contribution of G on the frontier molecular orbitals. (iv) The geometrical distortion of the copper corroles directly impacted the magnetic response since it correlated the ligand field distortion and the overlapping of the corresponding magnetic orbitals. (v) Finally, the

exposed results suggest that aryl-substituted corroles at the *meso* positions support the augmented magnetic response of the hybrid system, while electrophilicity of hybrids acts to the detriment of the ferromagnetic coupling. Statistical correlation analysis supported the rationalization of the augmented magnetic response and the spin transfer phenomena, showing that spin transfer is related to kinetic and thermodynamic stability. Under the same scope, the geometrical distortion of the **CuN₄** core was associated with the spin transfer and the magnetic response, which is consistent with the well-known influence of the ligand field for transition metal complexes.

Computational Methods.

A Graphene structure (**G**, C₃₈₄H₄₈) was modeled using a zig-zag hexagonal nanosheet with a diameter of ~39 Å and an area of 2692 Å² (based on its electron density). This model was designed from the graphite crystalline structure^[71] (**Fig. 1a**). The electronic structure of the graphene model was validated by Density-of-State plot (**Fig. S9**) which matched with reported works of pristine graphene^[72–74]. The copper corroles (**CuC**) are substituted in 5, 10, and 15 positions, giving rise to **C1-C7** compounds (**Fig. 1b**). DFT calculations were performed using the ORCA4 program^[75], considering the unrestricted open-shell formalism. The hybrid functional B3LYP^[76,77] was used with the 6-31G* basis sets; the LANL2DZ quasi-relativistic pseudo-potential and basis set^[78] was adopted for Cu. Energies were corrected for dispersion using the DFT-D3BJ method^[79,80]. The level of theory was chosen in regard of an equilibrium between accuracy and computational cost, extensive magnetic studies of Ruiz et al. where is demonstrated that GGA functional present important deviation of magnetic coupling constant due to self-interaction error (or delocalization error)^[54,81,82]. To overcome this error, several studies have standardized the

hybrid functional B3LYP for these calculations which included the Hartree-Fock exchange. On the other hand, the combination of Gaussian basis set and B3LYP have demonstrated excellent results for magnetic properties calculations^[54]. Literature suggest TZVP basis set but the computational cost increase substantially if is compared with the combination LanL2DZ and 6-31G that also reached excellent results (see table V in ^[81] and Figure 1 in ^[82]), thus, reducing from ~20000 to ~12000 the gaussian primitive function the computational cost is equilibrated.

In spite of the high symmetry of the graphene and its flat potential energy surface, different local minima can be found ^[81,83]. We have tried conformational search of each **C-G** hybrid putting copper atom of corroles on three different sites on the center of graphene nanosheet: onto the center of benzene ring; onto the C-C bonds; and onto C atom of graphene. During the full relaxation, the **CuC** structures “creeped” on the graphene surface, getting similar or equivalent structures; then, we have chosen the minimum energy structure as representative.

The stability of the graphene and corroles isolated structures were evaluated using cohesive energy. Thus, $E_{\text{coh}} = [E_{\text{molecule}} - \sum n_i E(i)] / (\sum n_i)$; where E_{molecule} , n_i , and $E(i)$ are the total energy of the molecule, the number of i -atom and the total energy of i -atom forming the molecule, respectively. The cohesive energy is defined as the required energy to break atoms into atomic species and is demonstrated to be directly associated with the formation enthalpy to state the stability of a bulk material and cluster^[84,85], although enthalpy calculations are strongly more expensive computationally compared with cohesive energy calculations.

The global reactivity indexes [chemical potential (μ), electronic hardness (η), and electrophilicity (ω)] were calculated to evaluate the chemical stability of the proposed systems in relation to an external perturbation, using the Koopman's theorem: $\mu = \frac{1}{2} (E_L + E_H)$; $\eta = \frac{1}{2} (E_L - E_H)$; and, $\omega = \mu^2 / 2\eta$ ^[86], where E_L and E_H were calculated as the average between energies of α and β spin-orbitals.

The stability of corrole-graphene hybrids (**C-G**) was characterized by the adsorption energies (E_{ads}):

$$E_{\text{ads}} = E_{\text{C}} + E_{\text{G}} - E_{\text{C-G}} \quad (1)$$

Where E_{C} , E_{G} , and $E_{\text{C-G}}$ are the energy of the corrole, graphene, and corrole-graphene complexes, respectively, the higher values of E_{ads} stand for the more stable systems. Basis set superposition error (BSSE) were corrected using the counterpoise method^[87]. The adsorption energy was decomposed in terms of the interaction and preparation energy (ΔE_{int} and ΔE_{prep} , respectively) following the expression: $-E_{\text{ads}} = \Delta E_{\text{int}} + \Delta E_{\text{prep}}$. Where ΔE_{int} represents the stabilizing interaction between **C** and **G** in the complex, while ΔE_{prep} is the energy penalty because of the deformation of **G** and **C** occurred in the adsorption process.

The nature of the intermolecular interactions was explored using the Atoms in Molecules (AIM) analysis, which allows classifying the interaction by the electron density at the bond-critical-point (ρ_{BCP}) of the intermolecular interactions. Moreover, the reduced gradient method based on the Independent Gradient Model (IGM) was used to analyze electron density since this method allows for the differentiation between intermolecular and intramolecular interactions, the δg_{inter} descriptor, which uniquely defines intermolecular interaction regions based on the Laplacian of electron density ($\nabla^2 \rho$)^[88]. The $\nabla^2 \rho$ describes if

the electron density is depleted or concentrated, but a more specific analysis is depicted by the eigenvalues λ_i of the electron-density Hessian matrix, such that $\nabla^2\rho = \lambda_1 + \lambda_2 + \lambda_3$ ($\lambda_1 < \lambda_2 < \lambda_3$). Specifically, the value of λ_2 allow to classify the nature of interactions, such as: if $\lambda_2 < 0$, there is polar attractive interaction; $\lambda_2 > 0$, in the case of steric (repulsive) interaction; and $\lambda_2 \approx 0$ is proper for dispersive interactions, similarly to Non-Covalent Interactions analysis^[89,90]. The AIM and IGM analyzes were developed employing the Multiwfn 3.7 program^[91].

The magnetic properties of **C** and **C-G** systems were calculated by applying broken-symmetry approximation for both antiferromagnetic and ferromagnetic states (AFM and FM, respectively)^[92]. Therefore, each magnetic system's electronic structure was described by the unrestricted corresponding orbitals (UCOs)^[93,94], which describes the magnetic exchange pathways and the overlap between the corresponding magnetic orbitals. Next, the magnetic exchange coupling was described according to the Heisenberg-Dirac-Van Vleck spin Hamiltonian^[95] following the expression:

$$\hat{H} = - \sum_{1 \geq 2} J_{12} \hat{S}_1 \cdot \hat{S}_2 \quad (2)$$

Where the terms H corresponds to the spin Hamiltonian, J_{12} is the magnetic exchange coupling constant between fragments 1 and 2; \hat{S}_1 , and \hat{S}_2 are the spin operators for fragments 1 and 2, respectively. The approximate spin-projected/broken-symmetry approach has been used for transition metal complexes and organic diradical^[96-99], then the J values were calculated as following the expression^[100,101]

$$J = \frac{E_{HS} - E_{BS}}{\langle \hat{S}^2 \rangle_{HS} - \langle \hat{S}^2 \rangle_{BS}} \quad (3)$$

Thus, E_{HS} is the SCF total energy for the high spin state, and E_{BS} is the electronic energy for broken-symmetry (singlet) states relative to FM and AFM states. The terms $\langle \hat{S}^2 \rangle_{HS}$, and $\langle \hat{S}^2 \rangle_{BS}$ show the total spin for high-spin and broken symmetry states. The wavefunction's stability was analyzed to validate the got electronic states.

Last, the geometrical distortion from the coordination sphere (g_d) caused by the ligand field (respecting the ideal solids) was characterized through the Shape 2.1 program^[102]; thus, the g_d function is calculated as (Eq. 4):

$$g_d = \min \frac{\sum_{k=1}^N |Q_k - P_k|^2}{\sum_{k=1}^N |Q_k - Q_0|^2} \times 100 \quad (4)$$

In this sense, the g_d can be contrasted with the ideal polyhedron composed of N vertexes, where for $N=4$, the alternatives are square, tetrahedron, seesaw, and axially vacant trigonal bipyramid, with an ideal symmetry of D_{4h} , T_d , C_{2v} , and C_{3v} , respectively. The term Q_0 corresponds to the mass center; Q_k is the term of the coordinates for distorted vectors, while P_k is the term for vectors of a perfect solid. The limiting conditions are between $100 \geq g_d \geq 0$; thus, the lower values show that structures match the target symmetry, while the higher values suggest highly distorted structures^[103].

Acknowledgements

Authors acknowledge the Programa de Cooperación Científica ECOS-ANID project No. C19E07 supported by the Chilean Comisión Nacional de Investigación Científica y Tecnológica (CONICYT), the French Ministère de l'Enseignement Supérieur, de la Recherche et de l'Innovation (MESRI) and the French Ministère de l'Europe et des Affaires Étrangères (MEAE). L. S. Acknowledge to Fondecyt Iniciación N° 11181187. P.D. acknowledges to FONDECYT 1201173. D.C-A thanks the financial support of the

ANID FONDECYT/Regular #1210355 and ANID/FONDEQUIP EQM180180. Project supported by the Fund of Scientific and Technological Equipment, year 2018, code L318-04, Universidad Tecnológica Metropolitana. Powered@NLHPC: This research was partially supported by the supercomputing infrastructure of the NLHPC (ECM-02). K.W-A acknowledges the financial support of ANID/FONDECYT Postdoctorado project # 3200270.

There are no competing interests to declare by the authors of this article.

Reference

- [1] H. Wang, L. Wang, F.-S. Xiao, *ACS Cent. Sci.* **2020**, *6*, 1685–1697.
- [2] F. Limosani, F. Tessore, G. Di Carlo, A. Forni, P. Tagliatesta, *Materials (Basel)* **2021**, *14*, 4404.
- [3] M. Adnan, J. J. Baumberg, G. Vijaya Prakash, *Sci. Rep.* **2020**, *10*, 2615.
- [4] S. A. Didas, S. Choi, W. Chaikittisilp, C. W. Jones, *Acc. Chem. Res.* **2015**, *48*, 2680–2687.
- [5] J. Chu, P. Shi, W. Yan, J. Fu, Z. Yang, C. He, X. Deng, H. Liu, *Nanoscale* **2018**, *10*, 9547–9560.
- [6] W. Zuo, R. Li, C. Zhou, Y. Li, J. Xia, J. Liu, *Adv. Sci.* **2017**, *4*, 1–21.
- [7] G. Kickelbick, Ed. , *Hybrid Materials*, Wiley, **2006**.
- [8] F. Bonaccorso, L. Colombo, G. Yu, M. Stoller, V. Tozzini, A. C. Ferrari, R. S. Ruoff, V. Pellegrini, *Science (80-.)*. **2015**, *347*, 1246501.
- [9] G. Bottari, M. Á. Herranz, L. Wibmer, M. Volland, L. Rodríguez-Pérez, D. M. Guldi, A. Hirsch, N. Martín, F. D’Souza, T. Torres, *Chem. Soc. Rev.* **2017**, *46*, 4464–4500.
- [10] C.-B. Huang, S. Witomska, A. Aliprandi, M.-A. Stoeckel, M. Bonini, A. Ciesielski, P. Samorì, *Adv. Mater.* **2019**, *31*, 1804600.
- [11] Y. Xu, Z. Liu, X. Zhang, Y. Wang, J. Tian, Y. Huang, Y. Ma, X. Zhang, Y. Chen, *Adv. Mater.* **2009**, *21*, 1275–1279.
- [12] S. Yang, Y. Lin, X. Song, P. Zhang, L. Gao, *ACS Appl. Mater. Interfaces* **2015**, *7*, 17884–17892.

- [13] A. Wang, L. Long, W. Zhao, Y. Song, M. G. Humphrey, M. P. Cifuentes, X. Wu, Y. Fu, D. Zhang, X. Li, C. Zhang, *Carbon N. Y.* **2013**, *53*, 327–338.
- [14] D. Dasler, R. A. Schäfer, M. B. Minameyer, J. F. Hitzenberger, F. Hauke, T. Drewello, A. Hirsch, *J. Am. Chem. Soc.* **2017**, *139*, 11760–11765.
- [15] I. Kruusenberg, J. Mondal, L. Matisen, V. Sammelselg, K. Tammeveski, *Electrochem. commun.* **2013**, *33*, 18–22.
- [16] Q. Lu, Y. Zhang, S. Liu, *J. Mater. Chem. A* **2015**, *3*, 8552–8558.
- [17] B.-P. Jiang, L.-F. Hu, D.-J. Wang, S.-C. Ji, X.-C. Shen, H. Liang, *J. Mater. Chem. B* **2014**, *2*, 7141–7148.
- [18] E. Gacka, A. Wojcik, M. Mazurkiewicz-Pawlicka, A. Malolepszy, L. Stobiński, A. Kubas, G. L. Hug, B. Marciniak, A. Lewandowska-Andralojc, *J. Phys. Chem. C* **2019**, *123*, 3368–3380.
- [19] E. Gacka, G. Burdzinski, B. Marciniak, A. Kubas, A. Lewandowska-Andralojc, *Phys. Chem. Chem. Phys.* **2020**, *22*, 13456–13466.
- [20] T. Ding, E. A. Alemán, D. A. Modarelli, C. J. Ziegler, *J. Phys. Chem. A* **2005**, *109*, 7411–7417.
- [21] G. Lu, W. Lin, Y. Fang, W. Zhu, X. Ji, Z. Ou, *J. Porphyr. Phthalocyanines* **2011**, *15*, 1265–1274.
- [22] Y. Fang, Z. Ou, K. M. Kadish, *Chem. Rev.* **2017**, *117*, 3377–3419.
- [23] J. F. B. Barata, M. G. P. M. S. Neves, M. A. F. Faustino, A. C. Tomé, J. A. S. Cavaleiro, *Chem. Rev.* **2017**, *117*, 3192–3253.
- [24] A. Ghosh, *Chem. Rev.* **2017**, *117*, 3798–3881.
- [25] L.-G. Liu, Y.-M. Sun, Z.-Y. Liu, Y.-H. Liao, L. Zeng, Y. Ye, H.-Y. Liu, *Inorg. Chem.* **2021**, *60*, 2234–2245.
- [26] R. F. Einrem, A. B. Alemayehu, S. M. Borisov, A. Ghosh, O. A. Gederaas, *ACS Omega* **2020**, *5*, 10596–10601.
- [27] R. D. Teo, J. Y. Hwang, J. Termini, Z. Gross, H. B. Gray, *Chem. Rev.* **2017**, *117*, 2711–2729.
- [28] J.-M. Barbe, G. Canard, S. Brandès, R. Guillard, *Chem. - A Eur. J.* **2007**, *13*, 2118–2129.
- [29] Y.-J. Lin, W.-Z. Cao, T. Ou Yang, C.-H. Feng, C.-T. Chang, *Sustain. Environ. Res.* **2019**, *29*, 22.
- [30] F. Cai, F. Xia, Y. Guo, W. Zhu, B. Fu, X. Liang, S. Wang, Z. Cai, H. Xu, *New J. Chem.* **2019**, *43*, 18012–18017.
- [31] A. Agresti, B. Berionni Berna, S. Pescetelli, A. Catini, F. Menchini, C. Di Natale, R. Paollesse, A. Di Carlo, *Adv. Funct. Mater.* **2020**, *30*, 2003790.

- [32] B. Mondal, K. Sengupta, A. Rana, A. Mahammed, M. Botoshansky, S. G. Dey, Z. Gross, A. Dey, *Inorg. Chem.* **2013**, *52*, 3381–3387.
- [33] H. Lei, C. Liu, Z. Wang, Z. Zhang, M. Zhang, X. Chang, W. Zhang, R. Cao, *ACS Catal.* **2016**, *6*, 6429–6437.
- [34] K. Sudhakar, A. Mahammed, Q.-C. Chen, N. Fridman, B. Tumanskii, Z. Gross, *ACS Appl. Energy Mater.* **2020**, *3*, 2828–2836.
- [35] S. Nardis, D. Monti, R. Paolesse, *Mini. Rev. Org. Chem.* **2005**, *2*, 355–374.
- [36] R. Orłowski, D. Gryko, D. T. Gryko, *Chem. Rev.* **2017**, *117*, 3102–3137.
- [37] D. T. Gryko, *J. Porphyr. Phthalocyanines* **2008**, *12*, 906–917.
- [38] G. Canard, D. Gao, A. D’Aléo, M. Giorgi, F.-X. Dang, T. S. Balaban, *Chem. - A Eur. J.* **2015**, *21*, 7760–7771.
- [39] S. Ye, T. Tuttle, E. Bill, L. Simkhovich, Z. Gross, W. Thiel, F. Neese, *Chem. - A Eur. J.* **2008**, *14*, 10839–10851.
- [40] H.-K. Norheim, J. Capar, R. F. Einrem, K. J. Gagnon, C. M. Beavers, H. Vazquez-Lima, A. Ghosh, *Dalt. Trans.* **2016**, *45*, 681–689.
- [41] A. B. Alemayehu, E. Gonzalez, L. K. Hansen, A. Ghosh, *Inorg. Chem.* **2009**, *48*, 7794–7799.
- [42] C. M. Lemon, M. Huynh, A. G. Maher, B. L. Anderson, E. D. Bloch, D. C. Powers, D. G. Nocera, *Angew. Chemie* **2016**, *128*, 2216–2220.
- [43] I. M. DiMucci, J. T. Lukens, S. Chatterjee, K. M. Carsch, C. J. Titus, S. J. Lee, D. Nordlund, T. A. Betley, S. N. MacMillan, K. M. Lancaster, *J. Am. Chem. Soc.* **2019**, *141*, 18508–18520.
- [44] K. Pierloot, H. Zhao, S. Vancoillie, *Inorg. Chem.* **2010**, *49*, 10316–10329.
- [45] W. Kaim, B. Schwederski, *Coord. Chem. Rev.* **2010**, *254*, 1580–1588.
- [46] Y. K. Maurya, K. Noda, K. Yamasumi, S. Mori, T. Uchiyama, K. Kamitani, T. Hirai, K. Ninomiya, M. Nishibori, Y. Hori, Y. Shiota, K. Yoshizawa, M. Ishida, H. Furuta, *J. Am. Chem. Soc.* **2018**, *140*, 6883–6892.
- [47] M. Kosa, N. Levy, L. Elbaz, D. T. Major, *J. Phys. Chem. C* **2018**, *122*, 17686–17694.
- [48] X. Li, H. Lei, X. Guo, X. Zhao, S. Ding, X. Gao, W. Zhang, R. Cao, *ChemSusChem* **2017**, *10*, 4632–4641.
- [49] F. Wu, J. Liu, P. Mishra, T. Komeda, J. Mack, Y. Chang, N. Kobayashi, Z. Shen, *Nat. Commun.* **2015**, *6*, 7547.
- [50] K. E. Thomas, H. Vazquez-Lima, Y. Fang, Y. Song, K. J. Gagnon, C. M. Beavers, K. M. Kadish, A. Ghosh, *Chem. - A Eur. J.* **2015**, *21*, 16839–16847.
- [51] K. Sudhakar, A. Mahammed, N. Fridman, Z. Gross, *Dalt. Trans.* **2019**, *48*, 4798–

4810.

- [52] H. Lei, H. Fang, Y. Han, W. Lai, X. Fu, R. Cao, *ACS Catal.* **2015**, *5*, 5145–5153.
- [53] M. Soll, K. Sudhakar, N. Fridman, A. Müller, B. Röder, Z. Gross, *Org. Lett.* **2016**, *18*, 5840–5843.
- [54] E. Ruiz, A. Rodríguez-Forteza, J. Tercero, T. Cauchy, C. Massobrio, *J. Chem. Phys.* **2005**, *123*, DOI 10.1063/1.1999631.
- [55] A. K. Seguin, K. Wrighton-Araneda, D. Cortés-Arriagada, C. Cruz, D. Venegas-Yazigi, V. Paredes-García, *J. Mol. Struct.* **2021**, *1224*, 129172.
- [56] S. Jana, P. Aich, P. A. Kumar, O. K. Forslund, E. Nocerino, V. Pomjakushin, M. Månsson, Y. Sassa, P. Svedlindh, O. Karis, V. Siruguri, S. Ray, *Sci. Rep.* **2019**, *9*, 1–10.
- [57] Y. Naruse, A. Takamori, *ChemRxiv* **2021**.
- [58] S. Ooi, T. Tanaka, T. Ikeue, K. Yamasumi, K. Ueta, D. Shimizu, M. Ishida, H. Furuta, A. Osuka, *Chem. – An Asian J.* **2019**, *14*, 1771–1776.
- [59] S. Ganguly, A. Ghosh, *Acc. Chem. Res.* **2019**, *52*, 2003–2014.
- [60] C. I. M. Santos, L. Rodríguez-Pérez, G. Gonçalves, S. N. Pinto, M. Melle-Franco, P. A. A. P. Marques, M. A. F. Faustino, M. Á. Herranz, N. Martin, M. G. P. M. S. Neves, J. M. G. Martinho, E. M. S. Maçôas, *Carbon N. Y.* **2020**, *166*, 164–174.
- [61] M. Paszkiewicz, T. Biktagirov, H. Aldahhak, F. Allegretti, E. Rauls, W. Schöfberger, W. G. Schmidt, J. V. Barth, U. Gerstmann, F. Klappenberger, *J. Phys. Chem. Lett.* **2018**, *9*, 6412–6420.
- [62] M. Zugermeier, J. Herritsch, J.-N. Luy, M. Chen, B. P. Klein, F. Niefind, P. Schweyen, M. Bröring, M. Schmid, R. Tonner, J. M. Gottfried, *J. Phys. Chem. C* **2020**, *124*, 13825–13836.
- [63] J. Xu, L. Zhu, H. Gao, C. Li, M. Zhu, Z. Jia, X. Zhu, Y. Zhao, S. Li, F. Wu, Z. Shen, *Angew. Chemie Int. Ed.* **2021**, *60*, 11702–11706.
- [64] D. P. Miller, J. Hooper, S. Simpson, P. S. Costa, N. Tymińska, S. M. McDonnell, J. A. Bennett, A. Enders, E. Zurek, *J. Phys. Chem. C* **2016**, *120*, 29173–29181.
- [65] N. Saikia, M. Seel, R. Pandey, *J. Phys. Chem. C* **2016**, *120*, 20323–20332.
- [66] J. Tang, B. Chen, Y. Zhang, J. Lu, T. Zhang, Q. Guo, J. Zhang, *Funct. Mater. Lett.* **2019**, *12*, 1940001.
- [67] S. Tebi, M. Paszkiewicz, H. Aldahhak, F. Allegretti, S. Gonglach, M. Haas, M. Waser, P. S. Deimel, P. C. Aguilar, Y.-Q. Zhang, A. C. Papageorgiou, D. A. Duncan, J. V. Barth, W. G. Schmidt, R. Koch, U. Gerstmann, E. Rauls, F. Klappenberger, W. Schöfberger, S. Müllegger, *ACS Nano* **2017**, *11*, 3383–3391.
- [68] Y.-W. Son, M. L. Cohen, S. G. Louie, *Nature* **2006**, *444*, 347–349.

- [69] Z. F. Wang, S. Jin, F. Liu, *Phys. Rev. Lett.* **2013**, *111*, 1–5.
- [70] A. Mugarza, C. Krull, R. Robles, S. Stepanow, G. Ceballos, P. Gambardella, *Nat. Commun.* **2011**, *2*, 490.
- [71] J. Zemann, *Acta Crystallogr.* **1965**, *18*, 139–139.
- [72] F. Joucken, Y. Tison, J. Lagoute, J. Dumont, D. Cabosart, B. Zheng, V. Repain, C. Chacon, Y. Girard, A. R. Botello-Méndez, S. Rousset, R. Sporcken, J.-C. Charlier, L. Henrard, *Phys. Rev. B* **2012**, *85*, 161408.
- [73] H. S. Moon, J. H. Lee, S. Kwon, I. T. Kim, S. G. Lee, *Carbon Lett.* **2015**, *16*, 116–120.
- [74] F. Joucken, L. Henrard, J. Lagoute, *Phys. Rev. Mater.* **2019**, *3*, 110301.
- [75] F. Neese, *Wiley Interdiscip. Rev. Comput. Mol. Sci.* **2018**, *8*, 4–9.
- [76] A. D. Becke, *J. Chem. Phys.* **1993**, *98*, 5648–5652.
- [77] C. Lee, W. Yang, R. G. Parr, *Phys. Rev. B* **1988**, *37*, 785–789.
- [78] P. J. Hay, W. R. Wadt, *J. Chem. Phys.* **1985**, *82*, 299–310.
- [79] S. Grimme, J. Antony, S. Ehrlich, H. Krieg, *J. Chem. Phys.* **2010**, *132*, 154104.
- [80] S. Grimme, S. Ehrlich, L. Goerigk, *J. Comput. Chem.* **2011**, *32*, 1456–1465.
- [81] E. Ruiz, S. Alvarez, J. Cano, V. Polo, *J. Chem. Phys.* **2005**, *123*, 1–7.
- [82] E. Ruiz, P. Alemany, S. Alvarez, J. Cano, *J. Am. Chem. Soc.* **1997**, *119*, 1297–1303.
- [83] I. Cimatti, L. Bondi, G. Serrano, L. Malavolti, B. Cortigiani, E. Velez-Fort, D. Betto, A. Ouerghi, N. B. Brookes, S. Loth, M. Mannini, F. Totti, R. Sessoli, *Nanoscale Horizons* **2019**, *4*, 1202–1210.
- [84] L. Glasser, D. A. Sheppard, *Inorg. Chem.* **2016**, *55*, 7103–7110.
- [85] M. Böyükata, J. C. Belchior, *J. Braz. Chem. Soc.* **2008**, *19*, 884–893.
- [86] P. Geerlings, F. De Proft, W. Langenaeker, *Chem. Rev.* **2003**, *103*, 1793–1874.
- [87] S. F. Boys, F. Bernardi, *Mol. Phys.* **1970**, *19*, 553–566.
- [88] C. Lefebvre, G. Rubez, H. Khartabil, J.-C. Boisson, J. Contreras-García, E. Hénon, *Phys. Chem. Chem. Phys.* **2017**, *19*, 17928–17936.
- [89] J. Contreras-García, E. R. Johnson, S. Keinan, R. Chaudret, J. Piquemal, D. N. Beratan, W. Yang, *J. Chem. Theory Comput.* **2011**, *7*, 625–632.
- [90] R. Laplaza, F. Peccati, R. A. Boto, C. Quan, A. Carbone, J. Piquemal, Y. Maday, J. Contreras-García, *WIREs Comput. Mol. Sci.* **2021**, *11*, 1–18.
- [91] T. Lu, F. Chen, *J. Comput. Chem.* **2012**, *33*, 580–592.
- [92] L. Noodleman, E. R. Davidson, *Chem. Phys.* **1986**, *109*, 131–143.

- [93] S. X. Cui, H. Y. Wang, J. Xu, J. P. Zhang, *Russ. J. Phys. Chem. A* **2017**, *91*, 1070–1075.
- [94] J. Svorec, P. Polakovičová, J. Moncol, V. Kuchtanin, M. Breza, S. Šoralová, Z. Padělková, J. Mrozinski, T. Lis, P. Segl'a, *Polyhedron* **2014**, *81*, 216–226.
- [95] J. H. Van Vleck, *Rev. Mod. Phys.* **1978**, *50*, 181–189.
- [96] A. Bencini, F. Totti, *J. Chem. Theory Comput.* **2009**, *5*, 144–154.
- [97] Y. Kitagawa, T. Saito, K. Yamaguchi, in *Symmetry (Gr. Theory) Math. Treat. Chem.*, InTech, **2018**.
- [98] Y. Kitagawa, T. Saito, Y. Nakanishi, M. Ito, M. Shoji, K. Koizumi, S. Yamanaka, T. Kawakami, M. Okumura, K. Yamaguchi, *AIP Conf. Proc.* **2007**, *963*, 334–337.
- [99] T. Saito, Y. Kataoka, Y. Nakanishi, T. Matsui, Y. Kitagawa, T. Kawakami, M. Okumura, K. Yamaguchi, *Chem. Phys.* **2010**, *368*, 1–6.
- [100] K. Yamaguchi, Y. Takahara, T. Fueno, in *Appl. Quantum Chem.*, Springer Netherlands, Dordrecht, **1986**, pp. 155–184.
- [101] T. Soda, Y. Kitagawa, T. Onishi, Y. Takano, Y. Shigeta, H. Nagao, Y. Yoshioka, K. Yamaguchi, *Chem. Phys. Lett.* **2000**, *319*, 223–230.
- [102] S. Alvarez, D. Avnir, M. Llunell, M. Pinsky, *New J. Chem.* **2002**, *26*, 996–1009.
- [103] S. Alvarez, M. Llunell, *J. Chem. Soc. Dalt. Trans.* **2000**, 3288–3303.